Dynamical Systems in Pin Mixers of Single-Screw Extruders

W. R. Hwang, K. W. Kang and T. H. Kwon
Dept. of Mechanical Engineering, Pohang University of Science and Technology, San 31, Hyoja-dong, Pohang, Kyungbuk, 790-784, South Korea

DOI 10.1002/aic.10130
Published online in Wiley InterScience (www.interscience.wiley.com).

Dynamical systems generated by various types of pin mixers were studied for the application to the single-screw extruders. A periodic unit of the pin mixer was modeled as a dynamical system of the complex duct flow. It was found that the cross-sectional space could be divided into two distinct regions: the inner and outer zones. The pin configuration directly affects the motion of fluid particles in the inner region, while motion in the outer region is governed by the resonance phenomena. The effects of the number of pins, the pin height, the pin orientation, and the composition of two different pin units were studied with the numerical results and explained in the language of the dynamical systems theories. Finally, the validity of our modeling, and the numerical result was verified by qualitative comparison with experimental results. © 2004 American Institute of Chemical Engineers *AIChE J,* 50: 1372–1385, 2004

Keywords: dynamical systems, single-screw extruder, pin mixer, fluid mixing, flow visualization.

Introduction

The pin mixer is a popular mixing device in the single-screw extrusion industry. It is easy to operate and to manufacture, but the mixing performance has been considered just moderate (Rauwendaal, 1991). Erwin and Mokhtarian (1980) studied the mixing performance of the pin mixer via the quasi-three-dimensional (3-D) analysis, and they explained that the reorientation of the material line is the major mixing mechanism. Yao et al. (2001) analyzed the mixing performance of the pin mixer, and their modification through the 3-D numerical study. However, we still have a few fundamental questions on the mixing mechanism of the pin mixers: such as (a) the role of a single pin on the collective motion of fluid particles over the whole domain, or (b) the effect of the number of the pins and the pin configuration on the motion of fluid particles and, thereby, on the mixing performance. In this study, we attempted to resolve these questions with the help of the classical dynamical systems theory and tools. Our objectives are to analyze the dynamical systems structures in the pin mixer and to understand mixing mechanisms, and finally to suggest an efficient pin configuration for good mixing. The pin configuration of this study includes the number of the pin, the height of the pin, the alignment angle, and the composition of two different pin units. Figure 1 shows the schematic description for the pin mixer in this study.

Highly viscous flows in the metering section of the single-screw extruder can be cast into the regular duct flow, and the flow in this category can be decoupled into the cross-sectional and the longitudinal flows, which play the roles of mixing and pumping, respectively (Kusch and Ottino 1992). Suppose the flow preserves the volume in 3-D, then the cross-sectional continuity is satisfied as well in the regular duct flow, and the fluid particle motion can be described with the stream function Ψ

$$\dot{x} = u = \frac{\partial \Psi(x, y)}{\partial y}, \dot{y} = v = -\frac{\partial \Psi(x, y)}{\partial x}, \dot{z} = w(x, y) \quad (1)$$

where (x, y, z) and (u, v, w) are the position of the fluid particle and the fluid velocity, respectively. The flow satisfying Eq. 1 is

Current address of W.R. Hwang: Materials Technology, Eindhoven University of Technology, Eindhoven, The Netherlands (Email: w.r.hwang@tue.nl).
Correspondence concerning this article should be addressed to T. H. Kwon at thkwon@postech.ac.kr.

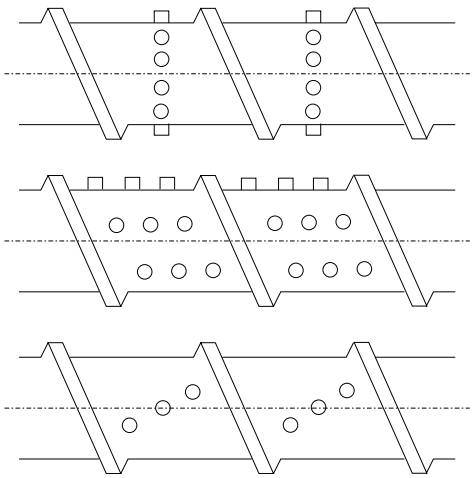

Figure 1. Various types of the pin mixer in single-screw extruders (Rauwendaal, 1991).

the 1-D Hamiltonian system, and the motion of a fluid particle is restricted to the stream surface determined by the initial position. In this regard, the flow in the metering section of the single-screw extruder is integrable. The integrability can be broken either by time-periodic or by spatially periodic changes of the cross-sectional flow, which can improve the mixing performance (Kusch and Ottino, 1992; Mezić and Wiggins, 1994). For flows in the single-screw extruder, the latter one can be achieved simply by changing the geometry of the screw surface (Jana et al., 1994; Kim and Kwon 1996). Indeed, flows in the pin mixer can be viewed as a complex duct flow, that is, a composite of the regular duct flow, and the perturbed flow due to the presence of the pin.

Recently, the classical dynamical systems theories have been successfully applied by the authors to understand the mixing mechanisms of complex flows in the single-screw extruder which has periodical geometric changes on the screw surface. In their previous studies, flows in a periodic unit were modeled as a dynamical system (Hwang and Kwon 2000) and particle motions were described by a two-dimensional map which preserves volume and orientation (Hwang and Kwon 2003). They analyzed the appearance of the unmixed and partially mixed zones by studying invariance or resonance in dynamical systems (Hwang and Kwon 2002b), and discussed the volumetric transports using by the 3-D lobe dynamics (Hwang and Kwon, 2003). They interpreted experimental mixing patterns in terms of the dynamical systems theories (Hwang et al., 2002a). In this study, we apply such approaches to the popular pin mixer in the screw extrusion industry to understand the fundamental mixing mechanism. This article is organized as follows: First, we model a dynamical system for flows in the pin mixer and introduce the pin type for categorization of the pin configuration. We discuss symmetries in the particle motion, as well as in the Poincaré map for different pin types. Next, we characterize the integrable system by the frequency ratio and discuss the flow resistance of the pin mixer by measuring the fractional loss of the flow rate. Third, the dynamical structures of the various pin types are presented with the Poincaré sections, and we interpret the underlying mixing mechanism in terms of the dynamical systems theory. Finally, comparison will be made with experimental mixing patterns to verify the validity of our modeling and numerical results.

Modeling

Periodic unit and governing set of equations

A periodic unit of the pin mixer is described in Figure 2, which is the system of our interest, assuming that the pin mixer consist of a large number of such units. In this typical example, the unit possesses three square-prism-like pins in a row in the unwound screw channel. The xy plane is called the cross-sectional plane, and the z direction is the longitudinal direction throughout the study. We denote the height of the screw flight by H, the width of the screw root by W, the length of the periodic unit by L, the drag velocity by V_d, and the helix angle by α. The width and the height of the pin are denoted by c and h, respectively. We used the fixed values $W = 4H$, $L = 3H$ and $c = 0.4H$, but we selected three different values for the pin height, $h = 0.55H$, $0.7H$, and $0.9H$.

Neglecting the diffusion, the motion of a fluid particle is completely determined by the surrounding velocity field through the advection equation which constitutes the dynamical system

$$\dot{\mathbf{x}} = \mathbf{v}(\mathbf{x}; \boldsymbol{\alpha}, \boldsymbol{\kappa}, \mathbf{p}) \tag{2}$$

where κ is the ratio of the pressure flow to the drag flow, and p is a parameter for the pin configuration to be specified in the next section. The value κ represents the effect of the (adverse) pressure gradient. Since the velocity field depends on (α, κ, p), all of them have been considered as the parameters of the system.

We assume the Stokes flow to confine ourselves within kinematics of flow only. By introducing the height of the flight and the drag velocity component in the longitudinal direction as the characteristic length and velocity scales, respectively, one can introduce dimensionless variables

$$\mathbf{x}^* = \frac{\mathbf{x}}{H}, \quad \mathbf{v}^* = \frac{\mathbf{v}}{V_{dz}}, \quad t^* = \frac{V_{dz}}{H}t, \quad p^* = \frac{1}{\mu}\frac{H}{V_{dz}}p \tag{3}$$

where μ, p, t are the viscosity, the pressure and time. Omitting the superscript *, the equation of motion is given by

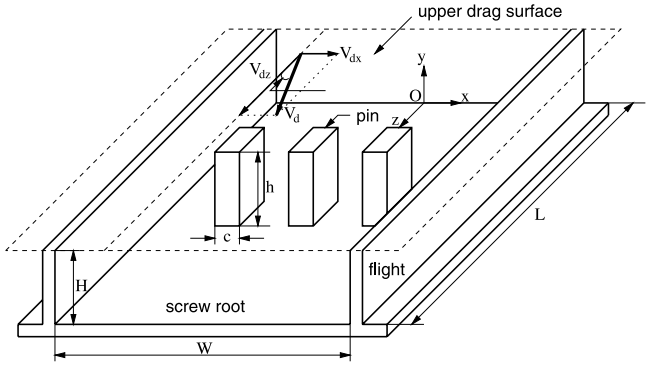

Figure 2. Periodic unit of a pin mixer in the unwound screw channel.

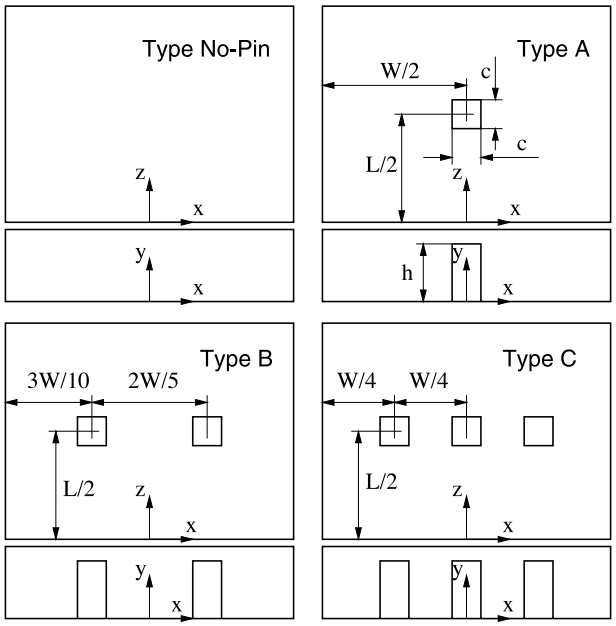

Figure 3. Basic pin types.

$$\nabla p = \nabla^2 \mathbf{v} \tag{4}$$

Neglecting the leakage flow over the clearance between the barrel surface and the flight, the boundary conditions are

$$\text{(i) On the upper drag surface: } \boldsymbol{v} = (\tan\alpha, 0, 1) \tag{5a}$$

$$\text{(ii) On the inlet and outlet surfaces: } \mathbf{v} = \mathbf{v}_0(x, y; \alpha, \kappa) \tag{5b}$$

$$\text{(iii) On the remaining boundaries: } \mathbf{v} = (0, 0, 0) \tag{5c}$$

where the velocity field of the no-pin case is denoted by $\mathbf{v}_0$, and it depends only on α and κ. By Eq. 5b, the velocity distribution on the inlet and outlet is assumed the no-pin flow solution.

Pin types and symmetry

In this study, the pin configuration, denoted by p, has been categorized into the "basic" pin types and the "modified" pin types for convenience. The basic pin types are distinguished by the number of the pin in a row, that is, the type A for the single pin case, the type B for two pins, and the type C for three pins (Figure 3). The modified pin types are grouped into three subclasses: (a) asymmetrically located pins; (b) pins oriented under a certain alignment angle θ; and (c) composites of two different basic pin types. The types A1 and A2 denote the asymmetric case (Figure 4a). The types C1 and C2 correspond to the second, which could be called "transversal" and "tangential", respectively (Figure 4b). The alignment angle is fixed by $\theta = \pi/6$ throughout the study. For the composite types, we denote the {-B-A-B-A-} configuration by the type A-B and the {-C-B-C-B-} by the type C-B (Figure 4c). The length of the periodic unit is $2L$ in the composite type.

From the geometrical symmetry, one can obtain the symmetry in the particle motion for all the pin types. The symmetry plays a significant role in constructing the Poincaré map, a tool for the visualization of dynamical systems structure. To do so, it is useful to define a periodic phase variable ϕ instead of the longitudinal coordinate z

$$\phi = \frac{z}{\lambda}, \quad \text{mod}(1) \tag{6}$$

where λ is the dimensionless spatial period L/H. Let us define the two reflection symmetries

$$\mathbf{S}_{xy} : (x, y, \phi) \mapsto (x, y, 1 - \phi), \quad \mathbf{S}_{y\phi} : (x, y, \phi) \mapsto (-x, y, \phi) \tag{7}$$

which satisfy the following identities with the identity transformation $\mathbf{I}$

$$\mathbf{S}_{xy}\mathbf{S}_{xy} = \mathbf{S}_{y\phi}\mathbf{S}_{y\phi} = \mathbf{I}, \quad \mathbf{S}_{xy}\mathbf{S}_{y\phi} = \mathbf{S}_{y\phi}\mathbf{S}_{xy} \tag{8}$$

The forward and backward time integrations during the infinitesimal time step δt can be expressed with a given particle position $\mathbf{p} = (x,y,\phi)$

$$\mathbf{Fp} = (x + u(\mathbf{p})\delta t, y + v(\mathbf{p})\delta t, \phi + w(\mathbf{p})\delta t) \tag{9a}$$

$$\mathbf{Bp} = (x - u(\mathbf{p})\delta t, y - v(\mathbf{p})\delta t, \phi - w(\mathbf{p})\delta t) \tag{9b}$$

The symmetry of a particle motion in the basic pin types during δt can be obtained from Eqs. 7–9, along with the symmetry in the velocity field (Eq. A1 in the Appendix) as follows

$$\mathbf{B} = \mathbf{S}_{xy}\mathbf{S}_{y\phi}\mathbf{F}\mathbf{S}_{y\phi}\mathbf{S}_{xy} \tag{10}$$

Equation 10 can be extended for a finite time step by the successive applications, and by Eq. 8

$$\mathbf{B}_n \cdots \mathbf{B}_1 = \mathbf{S}_{xy}\mathbf{S}_{y\phi}(\mathbf{F}_n \cdots \mathbf{F}_1)\mathbf{S}_{y\phi}\mathbf{S}_{xy} \tag{11}$$

Similarly, the symmetry for the asymmetric types (types A1 and A2) can be written as

$$\mathbf{B}_{A1} = \mathbf{S}_{xy}\mathbf{S}_{y\phi}\mathbf{F}_{A2}\mathbf{S}_{y\phi}\mathbf{S}_{xy}, \quad (\mathbf{B}_{A2} = \mathbf{S}_{xy}\mathbf{S}_{y\phi}\mathbf{F}_{A1}\mathbf{S}_{y\phi}\mathbf{S}_{xy}) \tag{12}$$

by using the symmetry in the velocity fields of this case (Eqs. A2 and A3 in the Appendix). Equation 12 can be also extended for the finite time step. Equation 12 implies that a particle motion in one type can be obtained from the other. One can end up with exactly the same symmetry relation of the type C1 and C2 as Eqs. 10 and 11 for the basic type, although their symmetry in the velocity field looks different (Eq. A4 in the Appendix). To get the symmetry in the composite type of the period 2λ, we introduce a new phase variable, $\bar{\phi}$,, slightly modified from ϕ, such that

$$\bar{\phi} = \frac{z}{2\lambda} + \frac{1}{4}, \quad \text{mod}(1) \tag{13}$$

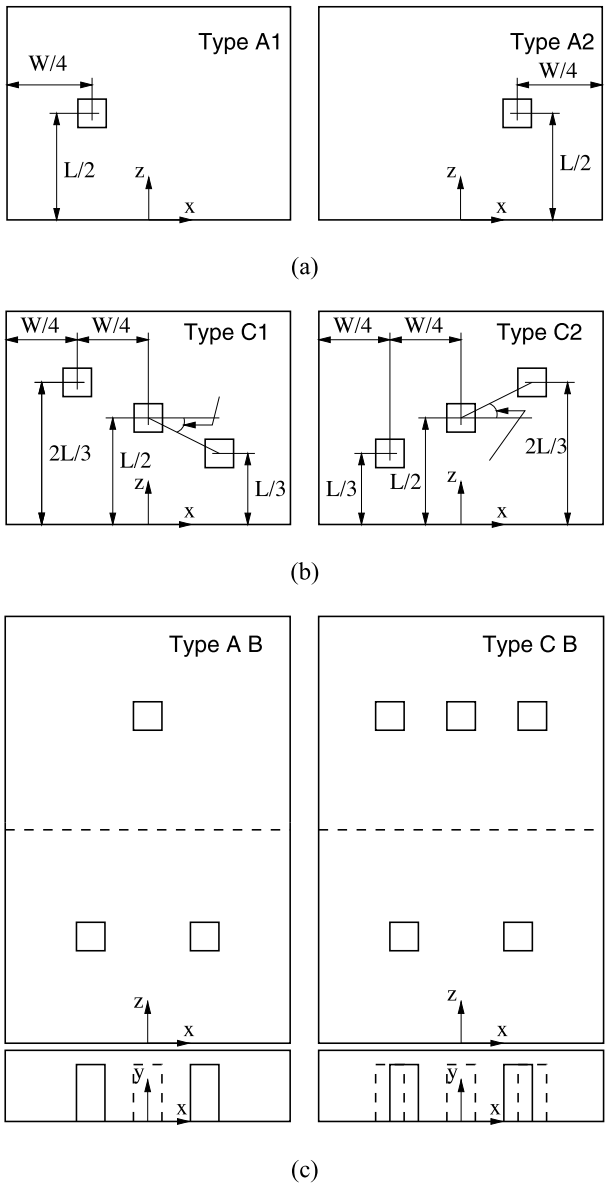

Figure 4. Modified pin types.

(a) Asymmetrically located pins; (b) the pins oriented under the angle θ; (c) the composites of two different pin types.

The value 1/4 has been added to attain the consistency in definition of the phase variable (Figure 5): for example, the reflection symmetry about the xy plane at $= 0$ and 1/2. The associated reflection symmetries are

$$\bar{\mathbf{S}}_{xy} : (x, y, \bar{\phi}) \mapsto (x, y, 1 - \bar{\phi}), \quad \mathbf{S}_{\bar{y}\bar{\phi}} : (x, y, \bar{\phi}) \mapsto (-x, y, \bar{\phi}) \tag{14}$$

Now the symmetry of a particle motion in the composite type can be written as

$$\mathbf{B} = \bar{\mathbf{S}}_{xy}\mathbf{S}_{\bar{y}\bar{\phi}}\mathbf{F}\mathbf{S}_{\bar{y}\bar{\phi}}\bar{\mathbf{S}}_{xy} \tag{15}$$

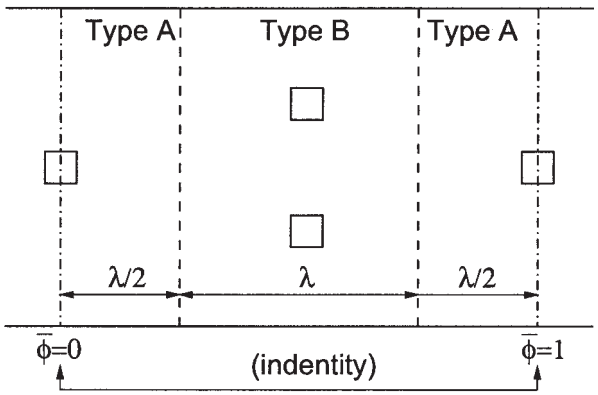

Figure 5. Phase variable $\bar{\phi}$ for the composite type.

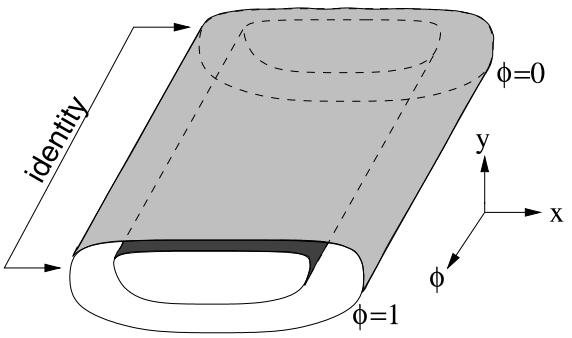

Figure 6. Description of the stream surface in the no-pin case.

which has the similar form as that of the basic type (Eq. 11). This analogy has come from the geometrical similarity of the two systems within ϕ (or $\bar{\phi}$) $\in$ [0, 1).

The Poincaré map

The cross-sectional Poincaré map, the best tool for visualization of dynamical systems in the complex duct flow, can be derived from the 2-D map, following the approach of Hwang and Kwon (2003). The 2-D map is a cross-sectional mapping along the flow

$$X(z) = \varphi(z, z_{0,sbx})X(z_0), \quad X=(x, y), \quad z>z_0 \tag{16}$$

which can be always defined under the transversal condition. The map preserves the flow rate and the orientation. The cross-sectional Poincaré map P, defined at the phase ϕ is

$$P_\phi : \Sigma_\phi \rightarrow \Sigma_\phi, \quad P_\phi \equiv \varphi(\lambda + \lambda\phi, \lambda\phi) \tag{17}$$

where is the cross-sectional plane at ϕ. The n-th iterate of the Poincaré map, and its inverse can be written as follows

$$P_\phi^{\pm n} = \varphi(\pm n\lambda + \lambda\phi, \lambda\phi) \tag{18}$$

The Poincaré map preserves the flow rate and orientation as well. Using Eq. 18 together with the symmetry of each pin type (Eqs. 10, 12, and 15), one can obtain the symmetry of the Poincaré map for all the pin types. For the types A, B, C, C1, and C2

$$P_{1-\phi}^{-n} = \mathbf{S}_y P_\phi^n \mathbf{S}_y \tag{19a}$$

where $\mathbf{S}_y : (x, y) \mapsto (-x, y)$.. For the asymmetric types A1 and A2

$$P_{1-\phi,\mathrm{A1}}^{-n} = \mathbf{S}_y P_{\phi,\mathrm{A2}}^n \mathbf{S}_y, \quad (P_{1-\phi,\mathrm{A2}}^{-n} = \mathbf{S}_y P_{\phi,\mathrm{A1}}^n \mathbf{S}_y) \tag{19b}$$

Finally, for the composite types, one gets

$$\bar{P}_{1-\bar{\phi}}^{-n} = \mathbf{S}_y \bar{P}_{\bar{\phi}}^n \mathbf{S}_y \tag{19c}$$

To investigate the longitudinal dynamical structures, one can use the longitudinal Poincaré section on a certain $y\phi$ plane defined by x. Since all the $y\phi$ planes are not transversal to the x-directional velocity component (in fact, only a part of the plane is transversal), care should be exercised in selecting the longitudinal section and in interpreting the results.

Flow Characteristics

Integrable system

The flow in the no-pin case is simply the regular duct flow and forms the integrable system. The dynamical structure is depicted in Figure 6. It consists of an infinite number of nested nonlinear rotations that can be characterized by the frequency ratio, the ratio of the two frequencies associated with the longitudinal rotation in the ϕ direction and with the cross-sectional rotation in the xy plane (Hwang and Kwon, 2000; Fountain et al., 2000). The frequency ratio plays a key role in understanding dynamics of the perturbed system induced by the presence of the pin. Later, we derive the expression of the frequency ratio following Hwang and Kwon (2002b).

In the no-pin case, the solution form of the velocity field can be obtained by the superposition of three simple flows: the unit drag flow, the unit cross-sectional flow, and the unit pressure driven flow. The unit drag flow $\mathbf{v}_d = (0, 0, w_d)$ is the flow generated by the upper drag velocity "1" in z; the unit cross-sectional flow $\mathbf{v}_c = (u_c, v_c, 0)$ is the result from the upper drag velocity "1" in x; and the unit pressure flow $\mathbf{v}_p = (0, 0, w_p)$ comes from a certain value of the pressure gradient that leads to the same amount of the flow rate from the unit drag, that is, $\int_\Sigma w_p dA = \int_\Sigma w_d dA$. Denoting the flow rates due to a pressure flow, and the unit drag flow by Q_p and Q_d, respectively, the parameter κ is defined as the ratio of the two with the minus sign, $\kappa = -Q_p/Q_d$, that is, the fraction of the back flow due to the pressure gradient. Now the no-pin velocity field can be expressed with α and κ as the parameters

$$\mathbf{v}_0(x, y; \alpha, \kappa) = \mathbf{v}_d(x, y) + \tan \alpha \mathbf{v}_c(x, y) - \kappa \mathbf{v}_p(x, y) \tag{20}$$

One can solve the unit flows by the finite-element method. Figure 7 shows the computed streamlines in the cross section. Thus, the frequency ratio Ω, a function of the stream surface, can be evaluated by the following formula (Hwang and Kwon 2002b)

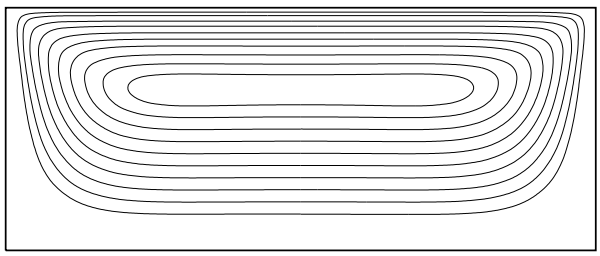

Figure 7. Cross-sectional streamlines for the no-pin case.

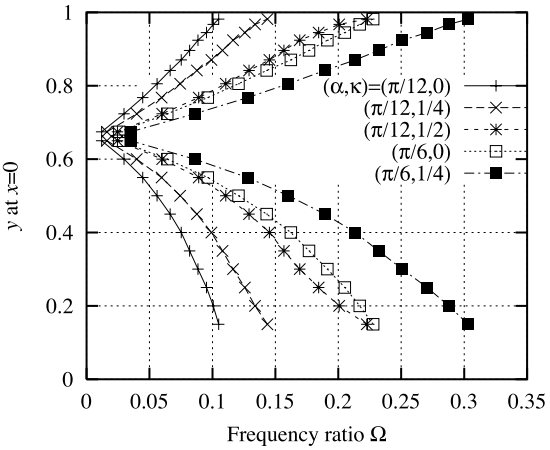

Figure 8. Frequency ratio distributions for several (α, κ) combinations.

$$\Omega(y|_{x=0};\ \alpha,\ \kappa) = \frac{\lambda \tan \alpha}{\int C[(w_d - \kappa w_p)(u_c^2 + v_c^2)^{1/2}]dl} \tag{21}$$

The y coordinate at $x = 0$ is used as the index for the stream surface and l is a coordinate defined along the (projected) cross-sectional rotation C. Plotted in Figure 8 is the frequency ratio distribution for several (α,κ) combinations. For the composite pin types with the period 2λ, the frequency ratio $\bar{\Omega}$ can be expressed as

$$\bar{\Omega}(y|_{x=0};\ \alpha,\ \kappa) = 2\Omega(y|_{x=0};\ \alpha,\ \kappa) \tag{22}$$

Flow resistance

The velocity fields of all the pin types have been solved by the finite element method. (see Hwang and Kwon (2000, 2002b)). Plotted in Figure 9 is an example of finite-element mesh used for the type A.

In general the mixing performance would increase with the number of the pin, while the throughput would decrease, due to the increased pressure drop Δp. It would be worthwhile to compare the pressure drops of difference types. Table 1 lists the computed pressure drop $\langle \Delta p, \rangle$ after taking the average over the cross section, for $\alpha = \pi/12$ and $\kappa = 0$. (Since $\kappa = 0$, $\langle \Delta p, \rangle = 0$ in the no-pin case.) Here, we introduce a measure of the flow resistance, the fractional loss of flow rate f_q, as follows

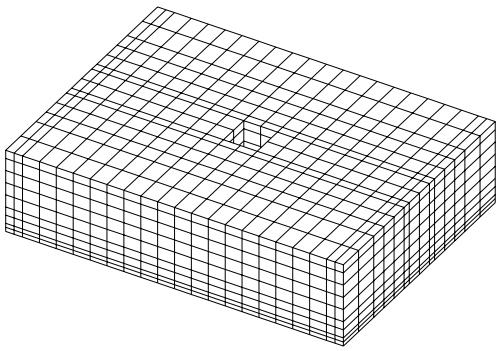

Figure 9. Example of finite element mesh for the type A with $h = 0.7$.

Table 1. The Fractional Loss of Flow Rate and the Averaged Pressure Drop for Several Types of the Pin Mixer (Evaluated for $\alpha = \pi/12$ and $\kappa = 0$)

Pin Type	Pin Height h	$\langle \Delta p \rangle$	f_q [%]
A	0.55H	1.56	7.78
A	0.7 H	2.27	10.9
A	0.9 H	3.09	14.3
B	0.55H	3.64	16.4
B	0.7 H	5.59	23.2
B	0.9 H	7.90	29.9
C	0.7 H	11.9	39.2
A1, A2	0.7 H	2.45	11.7
C1	0.7 H	9.74	34.5
C2	0.7 H	10.1	35.2
A–B	0.7 H	3.93	17.5
C–B	0.7 H	8.74	32.0
A–B*	0.9 H in A; 0.7 H in B	4.34	19.0

$$f_q = \frac{\langle \Delta p \rangle \hat{Q}_p}{Q_d + \langle \Delta p \rangle \hat{Q}_p} \tag{23}$$

where $\hat{Q}_p$ is the flow rate generated by the unit pressure drop in a single unit of the no-pin case. (Note that the flow rate of all the types is always Q_d due to the boundary condition Eq. 5b, with the zero κ value.) The denominator in Eq. 23 is the maximum possible flow rate for a given $\langle \Delta p, \rangle$, which can be realized in the no-pin case only. The numerator, the difference between the maximum possible flow rate and the actual flow rate Q_d, can be interpreted by the flow loss due to the presence of the pin. Thus, f_q in Eq. 23 has the meaning of the fractional loss of the flow rate. Table 1 lists the f_q values for all the pin types used in this study. The fractional loss in the composite type has been evaluated by taking the average of $\langle \Delta p, \rangle$'s of the two subunits, and then by applying Eq. 23.

Dynamical Systems

The dynamical systems structure can be best seen with the Poincaré section. In this study, all Poincaré sections have been obtained by the forward integration (Eq. 2) of about 100 initial points equally distributed at $\phi = 0$ for 200 periods, using the fourth-order Runge-Kutta method (RK4), with the time step 0.02. Then we applied the symmetry relations in Eqs.19a–c, to get backward integration results, which gives twice as many points on the section.

Basic pin types

Figure 10 shows the Poincaré sections at $\phi = 0$ and 1/2 for the type A with $\alpha = \pi/12$, $\kappa = 0$ and $h = 0.7$. The pin is centered at $\phi = 1/2$. There are two distinct regions separated by a KAM (Kolmogorov-Arnold-Moser) torus, which are called the inner and outer regions throughout the study. The inner region consists of one hyperbolic and two elliptic cycles (in 3-D) and dynamics, is quite regular except for small regions in the vicinity of the homoclinic connection. The existence of

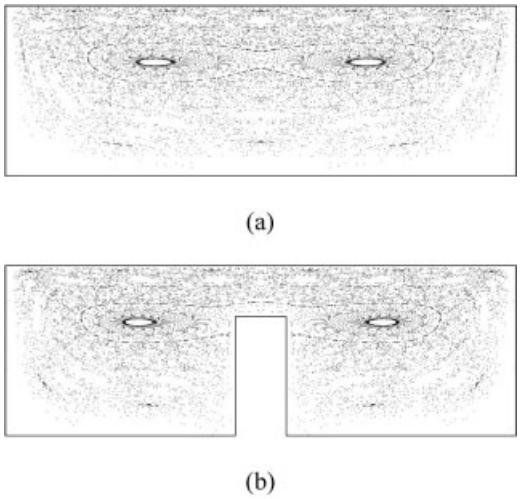

Figure 10. Poincaré sections at three different phases for the type A ($\alpha = \pi/12$, $\kappa = 0$, $h = 0.7$): (a) $\phi = 0$; (b) 1/2.

the pin exerts direct influence on the small-scale orbit in the inner region to produce the eyeglass shape of the dynamical structure. However, one can find coexistence of stochastic and

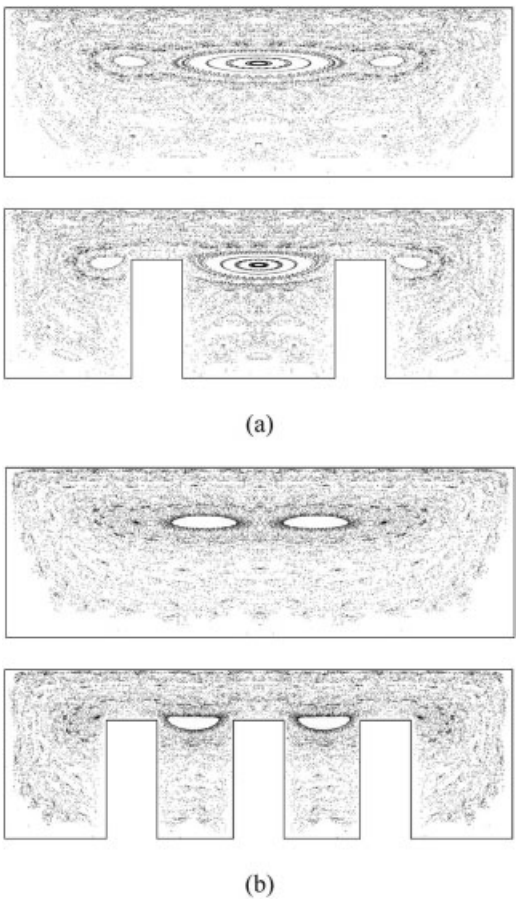

Figure 11. Poincaré sections at two different phases.

(a) the type B, and (b) the type C ($\alpha = \pi/12$, $\kappa = 0$ and $h = 0.7$). The phase $\phi = 0$ for the upper figures, and 1/2 for the lower ones.

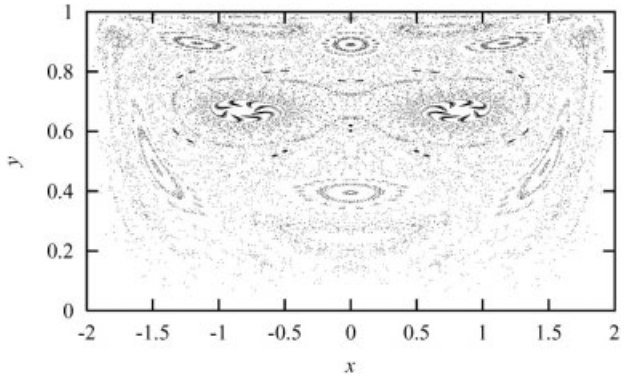

Figure 12. Poincaré section of the type A at $\phi = 0$ to show the dependence of resonance phenomena in the outer region on frequency ratios ($\alpha = \pi/6$, $\kappa = 0$ and $h = 0.7$).

regular regions with period-10 or higher resonance bands, which is a typical resonance structure. Therefore, the role of the pin for the large-scale orbits in the outer region can be identified as the perturbation.

The Poincaré sections for the types B and C are plotted in

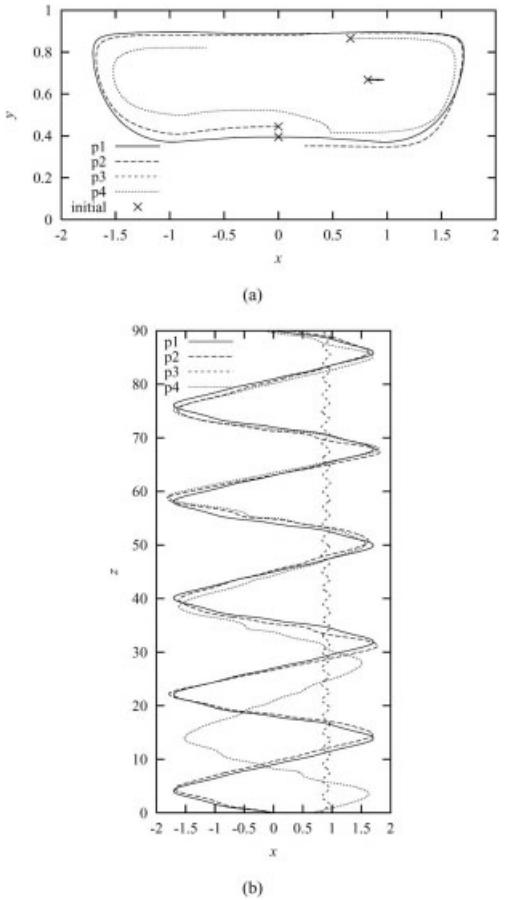

Figure 13: Orbits of the four particles from different initial locations possessing the different dynamical structures ($\alpha = \pi/6$, $\kappa = 0$ and $h = 0.7$).

(a) The cross-sectional orbits; (b) the longitudinal orbits.

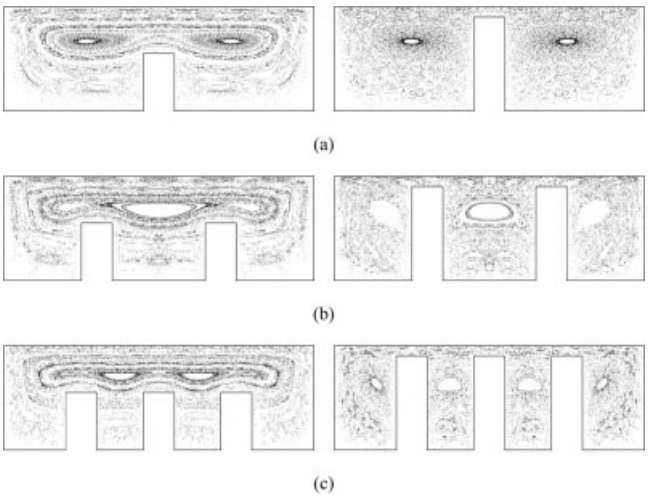

Figure 14. Poincaré sections evaluated at $\phi = 1/2$ for different pin heights h, and for different basic types ($\alpha = \pi/12$, $\kappa = 0$).

(a) Type A; (b) Type B; (c) Type C. The left figures are for $h = 0.55$, and the right ones are for 0.9.

Figure 1 at $\phi = 0$ and 1/2 with the same α and κ values previously. There appears to be a very high period resonance band dividing the inner region from the outer one in the Poincaré sections in both types, which plays the same role as the KAM torus in the previous example. In the inner region, one can observe three (one large and two small) elliptic rotations in the type B and four (two small and two large) elliptic rotations in the type C. Again, there can be found higher period resonance bands in the outer region and, comparing Figures 10 and 11, the size of the elliptic island inside the resonance band decreases with increasing the number of pins.

Resonance in outer region

The dependence of the resonance phenomena in the outer region on the frequency ratio has been investigated with a large value of the helix angle α, to achieve small denominators in the ratios and, thereby, to obtain apparent resonant structures. Plotted in Figure 12 is the Poincaré section of the type A at $\phi = 0$ with $\alpha = \pi/6$, $\kappa = 0$ and $h = 0.7$. From the frequency ratio in Figure 8, the dominant rational frequency ratios appear 1/5 (at $y = 0.27$), 1/6 (at 0.4), and 1/10 (at 0.54) along the $x = 0$ line. One can observe the period-5, 6, and 10 resonance bands at the right place in Figure 12.

Figures 13a and 13b show the cross-sectional and longitudinal trajectories of four particles whose initial locations belong to different dynamical structures in Figure 12. The cross-sectional orbits are plotted only up until z = 18 (6 λ) to avoid confusion. The material point denoted by p_1 is initially located at (x, y, z) = (0, 0.3937, 0), the elliptic rotation center of the period-6 resonance band. The orbit of p_1 shows a closed loop in the cross-sectional plane and, also, shows a periodic oscillation in the longitudinal plane with the period 6λ. The initial location (0, 0.4444, 0) of the point p_2 has been taken at the boundary of the island associated with the period-6 resonance band. The point follows the orbit of within a very short distance during the whole range of z, which can be considered as a typical subharmonic motion. The initial location of p_3 , (0.8231, 0.6678, 0), has been selected at the elliptic rotation center in the right half of the inner zone, and its orbit shows a periodic oscillation of the elliptic fixed point along the phase (Figure 13b). It is periodic with λ due to the geometric periodicity. The initial point p_4 at (0.6629, 0.6851, 0) is selected from the stochastic zone, and its orbit is affected directly by the pin. However, it is trapped soon after by the resonance band of period 6 (Figure 13b), and afterward the orbit follows the similar path as those of P_1 and P_2. In fact, the outer region is filled with many resonance bands and chaotic material orbit would originate from perturbed heteroclinic orbits in resonance bands. Thus, it can be easily trapped to be subharmonic motion through lobe motions in perturbed heteroclinic manifolds.

The pin height

Plotted in Figure 14 are the Poincaré sections at $\phi = 1/2$ of the types A, B and C, with two different pin heights, $h = 0.55$ and 0.9. The first observation is the existence of bounding KAM torus (or very high-order resonance bands) dividing the inner region from the outer one. There is no such structure in the case of $h = 0.9$ irrespective of the pin types, whereas one can find strong nested bounding KAM tori for all the $h = 0.55$ cases. Second, the pin height affects the size of the elliptic islands of the resonance band in the outer region. The size of the island decreases with the increment of h. As explained, the existence of pins can be regarded as a perturbation for orbits in the outer region. If the height of the pins is comparable to the height of the flight, this perturbation mechanism works twice in both upper and lower regions. Thus, the orbit undergoes the larger distortion that results in the smaller size of elliptic islands of the resonance band.

Pins arranged under the angle

Figure 15 shows the Poincaré sections for the types C1 (transversal) and C2 (tangential) with the alignment angle $\theta = \pi/6$ ($\alpha = \pi/12$, $\kappa = 0$). (In these examples, the Poincaré section at $\phi = 2/3$ can be obtained from the Poincaré section at $\phi = 1/3$ by applying the reflection symmetry about $x = 0$ from Eq. 19a.) Indeed dynamical systems of the two are distinct, but there is no significant difference in the location or the

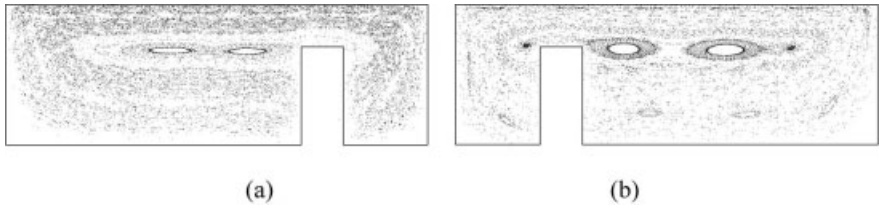

Figure 15. Poincaré sections for the types C1 and C2 ($\alpha = \pi/12$, $\kappa = 0$): (a) Type C1 at $\phi = 1/3$; (b) Type C2 at 1/3.

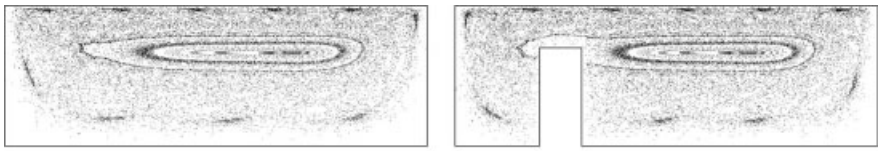

(a) (b)

Figure 16. Poincaré sections of the type A2 ($\alpha = \pi/12$, $\kappa = 0$): (a) $\phi = 0$; (b) 1/2.

size of the elliptic rotations: that is, four elliptic and three hyperbolic cycles in the inner region, and the resonance in the outer region, which are basically the same as that of the type C. The reason for this similarity might be two-fold. First, let us observe the Poincaré sections in Figure 16 for the asymmetric types A1 and A2, which are symmetric to each other from Eq. 19b. As shown Figure 16, the location of the pin in the screw width direction x determines the structure of dynamical systems in the inner region (over the whole range of ϕ) and, thereby, the longitudinal location of the pin can be considered less important. This observation explains the similarity of the dynamical structures in the inner region. The dynamical structure is determined by the number of the pins, and by their locations in the x direction, and the types C, C1 and C2 have all the same pin locations in the x direction. The dynamical similarity in the outer region can be understood through the resonance mechanism. Concerning the role of the pin, there is a disturbance on the orbit, and the important thing for this disturbance is not the location of the pin, but the number of the pins or size of pins. However, there seems a small practical advantage in using the types C1 and C2 rather than the type C. The alignment angle gives a bit less pressure drop compared with the all-pins-in-a-row case (Type C), as indicated in Table 1.

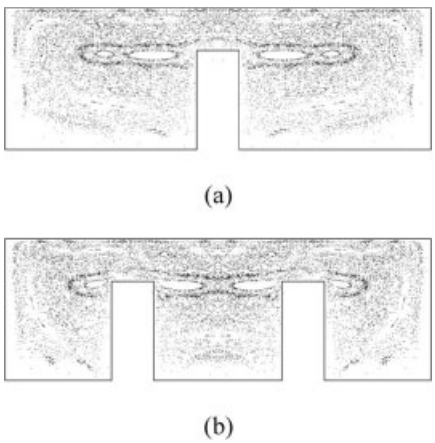

(a)

(b)

Figure 17. Poincaré sections for the type A-B ($\alpha = \pi/12$, $\kappa = 0$): (a) = 0; (b) 1/2.

The composite systems

The composites of two different pin types have been found to give better dynamical structures for mixing without excessive use of the flow resistance (Table 1). Plotted in Figure 17 are the Poincaré sections of the type A-B evaluated at the two different $\bar{\phi} = 0$ and 1/4. There are four elliptic cycles and three hyperbolic cycles in the inner region, which is similar to the three-pin cases, and the size of the elliptic rotations there becomes noticeably smaller than that of the type A or the type B (Figures 10 and 11a), yet the flow resistance of the type A-B is a bit larger than the type B with $h = 0.55$. The mechanism producing this preferable dynamical structure in the inner region can be explained as follows: the pin in the subtype A breaks the large elliptic island in the inner region of the subtype B, and the two pins in the subtype B break the two large elliptic islands of the subtype A. There can be observed period-6 and -7 resonance bands in the outer region, which is the result of the increased frequency ratio (by a factor of 2) in the composite systems (Eq. 22). The Poincaré sections of the type C-B are presented in Figure 18, and the result shows the similar dynamical structures as the type A-B, but the smaller size of the islands, both in the inner and outer regions.

Longitudinal structures

Figure 19 shows the longitudinal Poincaré section at the $x = 0$ plane ($\alpha = \pi/12$, $\kappa = 0$, $h = 0.7$ of Type A). The KAM torus forms the empty channel near $y = 0.7$. The upper and lower half planes, divided by about $y = 0.7$, are transversal to the velocity field so that each of the two can be used as the Poincaré sections. There can be seen one period-1 island in each transversal Poincaré section, since the corresponding reciprocal of the frequency ratio is an integer.

In the literatures of the pin mixer, one of the most frequently referred issues is the existence of dead spots behind the pin and at the 90 (deg.) between the pins and the root of the screw (Rauwendaal 1991). However, there can be observed no special

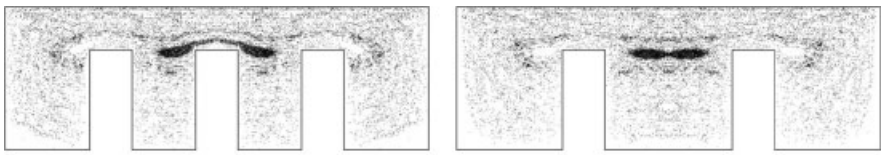

(a) (b)

Figure 18. Poincaré sections for the type C-B ($\alpha = \pi/12$, $\kappa = 0$): (a) = 0; (b) 1/2.

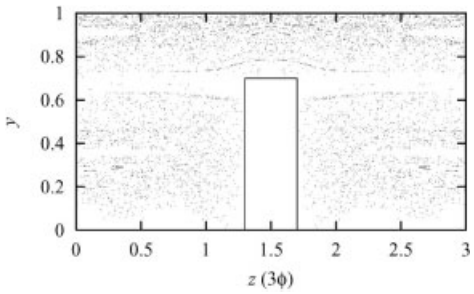

Figure 19. Longitudinal Poincaré section for the type A ($\alpha = \pi/12$, $\kappa = 0$) evaluated at the $x = 0$ plane.

structure that possibly induces such a dead spot in Figure 19, and as one can see in the next section, the experimental mixing pattern does not show such dead spots either. There is a slow velocity region near the pin, due to the no-slip walls of the pin and the screw root, which might increase the probability to observe agglomerations of the dye in the experiment, but it is not a dead spot because materials passing through it can be transported to other regions afterward. Simplifying materials to a Newtonian fluid might cause this disagreement with the previous observation.

Dead spots

It would be worthwhile to discuss briefly the apparent poor mixing regions, that is, the elliptic rotations in the inner zone, which should be avoided in design. Here we discuss mixing characteristics of such a region in the type B, as an example. As indicated in Figures 11a and 14b, there is a large elliptic rotation in the center of the inner zone, irrespective of h. Materials in the large region covered by this elliptic rotation are completely distinct from the others. Thus, the region forms a dead spot, and the mixing performance in the region would be unsatisfactory. We evaluated the length stretch to measure the mixing performance. The stretch ratio along the flow is defined by Ottino (1989)

$$\lambda_t = (\mathbf{M} \cdot \mathbf{C} \cdot \mathbf{M})^{1/2}, \quad \mathbf{C} = \mathbf{F}^T\mathbf{F} \tag{24}$$

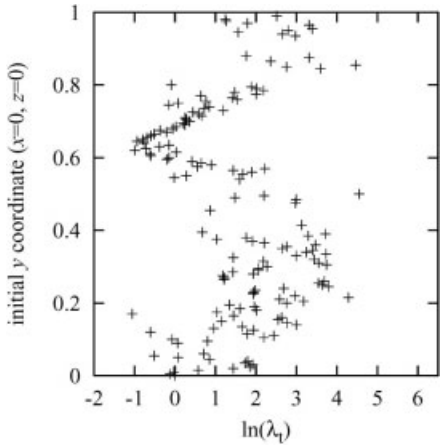

Figure 20. Logarithmic local rate of stretch for the type B with $h = 0.9$.

where $\mathbf{C}$, $\mathbf{F}$ and $\mathbf{M}$ are the green deformation tensor, the deformation gradient tensor and the initial orientation vector, respectively. The evolution of the tensor $\mathbf{F}$ is given by

$$\dot{\mathbf{F}} = \mathbf{L}(\mathbf{x})\mathbf{F}(\mathbf{x}), \quad \mathbf{F}|_{t=0} = \mathbf{I} \tag{25}$$

which should be solved in combination with Eq. 2. The tensor $\mathbf{L}$ denotes the transpose of the velocity gradient. By taking the initial orientation $\mathbf{M} = (1,0,0)$, parallel to the cross-sectional velocity, the stretch ratio λ_t becomes simply $(C_{11})^{1/2}$. Figure 20 shows the distribution of the logarithmic local length stretch ratios (in λ_t) of the type B with $h = 0.9$. The calculation has been carried out by using RK4, for t = 70 for initial 200 fluid particles located along the $x = 0$ axis, and the value is plotted with respect to the initial position y of the fluid particle. As shown in Figure 20, one can see very small values of the length stretch near $y = 0.6$. The region corresponds to the large elliptic rotations in the Poincaré section (Figure 14b), and it can be considered as a dead spot.

A good design

The parameter studies up until now can be summarized as follows: (a) The pin height h is important because a sufficiently high pin can break up the bounding KAM torus between inner and outer regions, and it gives additional disturbance to orbits in the outer region; (b) The orientation of the pin is not important; (c) the composition of the two different pin units is an excellent way to homogenize the dynamical structure by avoiding large dead spots without introducing the excessive pressure drop. On the basis of these results, we are now able to design a favorable pin mixer. We choose a composite type A-B with $h = 0.9$ in the subunit A and $h = 0.7$ in B. The idea lying behind this choice is that the tall pin in the type A breaks the KAM torus, as well as the large elliptic island in the inner region, which are generated by in the type B, and that the two small pins in the type B can break the large elliptic islands on the right and left half of the pin, which are produced by the type A. The Poincaré sections of this choice are plotted in Figure 21. There is no bounding KAM torus, and we get much smaller

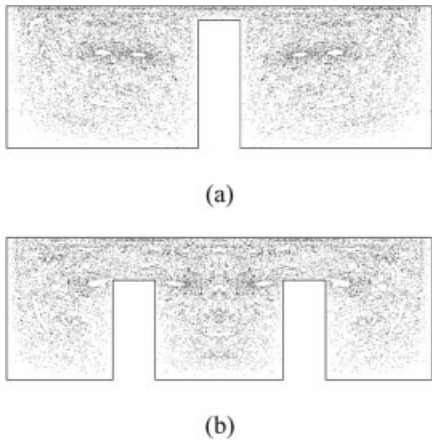

Figure 21. Poincaré sections for the optimal composition of the type A-B with h = 0.9 in the subunit A and $h = 0.7$ in B ($\alpha = \pi/12$, $\kappa = 0$). (a) = 0; (b) 1/2.

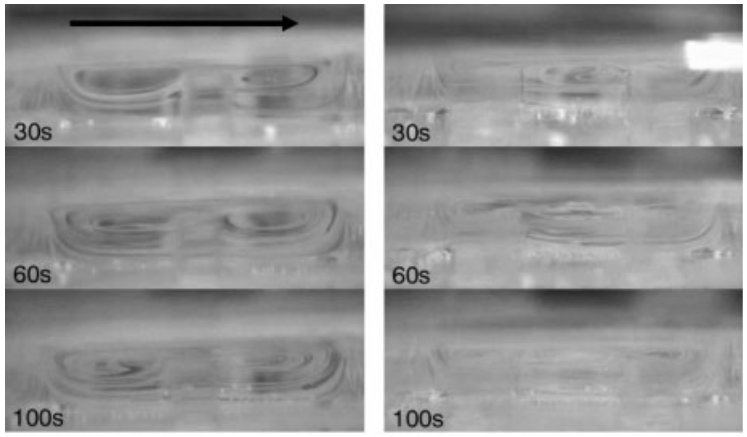

Figure 22. Experimental cross-sectional mixing patterns at t = 30s, 60s and 100s.

(a) Type A with $h = 0.7$; (b) Type B with $h = 0.7$. The arrow indicates the cross-sectional drag direction.

elliptic islands in the inner zone than the type A-B. The size of the island is as small as those in the resonance band in the outer region. In addition, the flow resistance of this composition is less than that of the type B with $h = 0.7$. Compare the Poincaré sections of the two (Figures 21 and 11a).

Experiments

Experimental procedures

We used the same experimental apparatus as the authors' previous work for visualizations of 3-D mixing patterns in the screw channel flow (Hwang et al., 2002a). The apparatus is composed of three major parts: (a) A transparent channel with the changeable upper plate and the motor driven slider; (b) two fluid reservoirs, a valve, and a drain system to keep the flow rate constant; (c) the image grabbing system. In the original design, we used several core barrier parts, which were fit with the fixed upper plate, to employ different geometries. However, in this study, the five different upper plates have been used for the same number of pin types: three for the type A with different pin heights, $h = 0.5H$, $0.7H$, $0.9H$; one for the type B with $h = 0.7H$; and the last one for the type A-B with $h = 0.9H$ in the subtype A and $0.7H$ in the subtype B. In the experiment, we used the pins with the circular cross section whose diameter is the same as the width of the square cross section c for convenience in manufacturing a large number of pins in the experiment, bearing in mind that the cross-sectional geometry of pins would not affect much on the dynamical behaviors. The height of the channel H is 0.03 m, the period of the channel L is 0.06 m ($2H$), and the width of the channel W is 0.12 m ($4H$). Each upper plate has 14 periodic units. The dye material was injected at the middle of the channel in the longitudinal direction, where the velocity field in the observing area is believed to be unaffected by the inlet and outlet.

The helix angle α is 70° and the drag velocity of the slider is 0.035 m/s. The choice of the large helix angle is to give many cross-sectional rotations in a limited length of the channel within a limited time of the experiment. We believe that the basic dynamical structures of the system will be the same, since

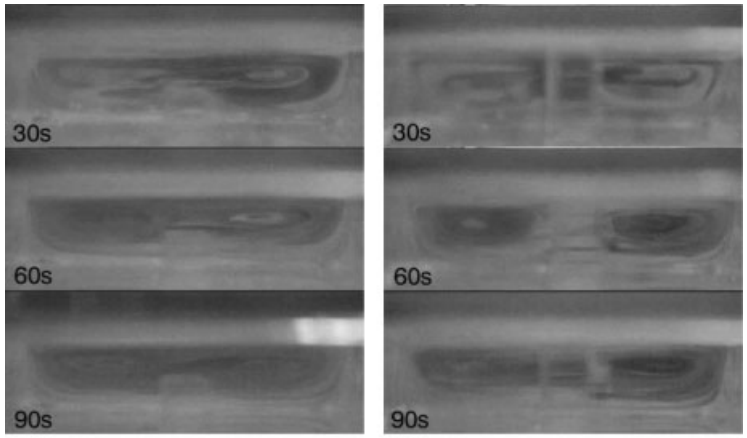

Figure 23. Experimental cross-sectional mixing patterns at t = 30s, 60s, and 90s.

(a) Type A with $h = 0.5$; (b) Type A with $h = 0.9$.

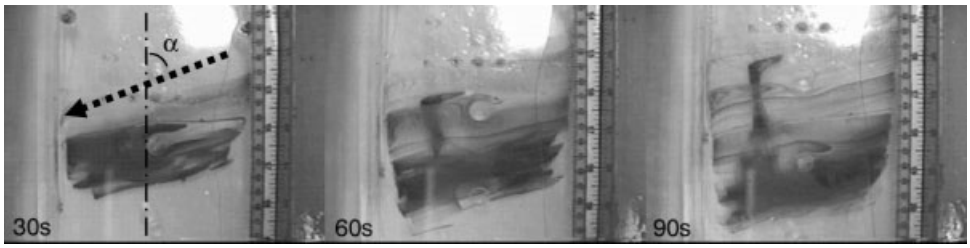

Figure 24. Experimental longitudinal mixing patterns of the Type A with $h = 0.5$ at t = 30s, 60s, and 90s.

The arrow indicates the drag direction.

the mechanism generating the inner and outer region dynamics does hold even with the large helix angle. As the working fluid, the silicone oil (Shinetsu Co. Japan) of the viscosity $\mu = 0.974$ Pa.s, and the density $\rho = 0.967 \times 10^{-3}$ kg/m^3 has been used. The dye material is the same silicone oil mixed with the color powder ($CoAlO_4$) of the size about 20 μm (KE BL70®), Shin-Etsu Co., Japan)and the diffusion coefficient D is estimated as 1.1×10^{-17} m^2/s. The Peclet number and the Reynolds number in the experiment are evaluated as follows

$$Pe = \frac{V_{dz}H}{D} = 0.93 \times 10^{14}, \quad Re = \frac{\rho V_{dz}H}{\mu} = 0.356$$

For details of the experimental procedures, refer to Hwang et al. (2002a).

Experimental results

All experimental deformation patterns have been presented for 100 s, about two and half period movement of the dye in the longitudinal direction. Since dynamical structures of the numerical Poincaré sections should be present even in a single periodic unit, the experiments during a few periods can be expected to reproduce such dynamical structures. In addition, the resonant motion in the outer zone is quite difficult to identify in the experimental mixing patterns, not only because of its size, but also due to its subharmonic nature. Therefore, we concentrate only on the dynamical structures of the inner zone in interpreting the experimental results.

Let us first observe the difference in the dynamical structure for the basic types. Figure 22a and 22b show the cross-sectional mixing patterns for the types A and B, respectively, both with $h = 0.7\ H$, at $t = 30$s, 60s, and 100s. In the type A, one can observe the eyeglass shape of the dynamical structures composed of two elliptic rotations in the right and left halves, which agrees with the numerical simulation (Figure 10). Again, for the type B, there can be observed three elliptic rotations in the inner zone, which is again consistent with the numerical results (Figure 11a).

The effect of the pin height can be observed in Figure 23, the cross-sectional mixing patterns of the type A with the two different pin heights, $h = 0.5$ and 0.9. The mixing patterns of the $h = 0.5$ case in Figure 23a, shows the thicker eyeglass shape than the $h = 0.7$ case (Figure 22a), and the $h = 0.9$ case (Figure 23b). The mixing patterns in the right and left halves appeared more separated in the taller pin case (Figure 23b). The inner zone of the small pin case is expected to consist of many nested bounding KAM tori, so that the elliptic rotations in the left and the right halves are comparably stable. Consequently, one can observe a KAM torus in the longitudinal mixing patterns of the $h = 0.5$ case (Figure 24). The KAM torus has come from the stable elliptic rotation in the left half of the cross-sectional mixing patterns (Figure 23a).

The cross-sectional mixing patterns for the composite type A-B with $h = 0.9$ in the subtype A and with 0.7 in the subtype B are presented in Figure 25. As mentioned in the previous section, this is a favorable design, since each pin in a subunit destroys a large elliptic rotation in the inner zone of the other subunit. In the first two subfigures (15s and 30s), the deformation of the dye is influenced by the subtype A, producing the

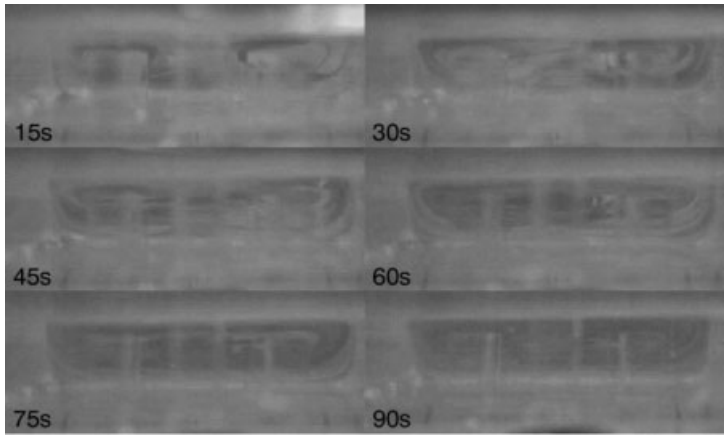

Figure 25. Experimental cross-sectional mixing patterns of the composite type A-B with $h = 0.9$ in the subtype A and with 0.7 in the subtype B.

similar mixing patterns of the type A composed of two large elliptic rotations. However, as the dye pass through the subtype B (from 45s to 75s), the two elliptic rotations were broken into small elliptic islands by the existence of two pins in the subtype B. There is no large elliptic rotation for either the subtype A or the subtype B in the final subfigure (90s), which agrees well with the corresponding numerical results in Figure 21.

Conclusions

We discussed the dynamical systems structures generated in the various types of the pin mixer through the dynamical systems modeling and the numerical simulations. The validity of our modeling and numerical results were verified by the qualitative comparison with the experimental mixing patterns. We interpreted the effects of the number of the pin, the pin height, the pin orientation, and the composition of the different pin units on the dynamical structures, and the mixing performance with the help of the dynamical systems theory.

Let us answer to the two fundamental questions raised in the beginning of this article based on the results of this work. The first question was about the role of a single pin on collective motions of fluid particles over the whole domain. The role of a single pin depends on the scale of fluid particle orbits. For the outer large-scaled orbits, the existence of the pin can be considered as a perturbation so that the resultant dynamical structures are affected by the resonance phenomena. However, for small-scaled orbits in the inner region, the pin directly affects the dynamical structures by generating elliptic rotations. The second question was about the effects of pin configuration - the number of the pin, the pin height, the orientation of pin arrangement, the composition, and so on. In the outer region, the number of the pin and the height of pins are related to the amount of perturbation and, thereby, affect size of elliptic rotations in resonance bands. For the same reason, the orientation of the pin arrangements, and the composition does not produce significantly different structures in the outer region. However, the inner region dynamics is highly dependent on the number of the pin, the pin height, and the composition. The number of pins determines the number of elliptic rotations; the height of pins affects existence of the bounding KAM torus; and a composite of two different units can break elliptic rotations effectively. However, the orientation does not give apparent difference, as long as the location of the pin in the screw width direction is unaltered.

Acknowledgment

This work was supported by the Ministry of Science and Technology of Korea via National Research Laboratory Program (2000-N-NL-C-148).

Literature Cited

Erwin, C., and F. Mokhatarian, "Analysis of Mixing in Modified Single-Screw Extruders," *Polym. Eng. Sci*., **23**, 49 (1983).

Fountain, G. O., D. V. Khakhar, I. Mezić, and J. M. Ottino, "Chaotic Mixing in a Bounded Three-Dimensional Flow," *J. Fluid Mech*., **417**, 265 (2000).

Hwang W. R., and T. H. Kwon, "Dynamical Modeling of Chaos Single-Screw Extruder and Its Three-Dimensional Numerical Analysis," *Polym. Eng. Sci*., **40**, 702 (2000).

Hwang, W. R., H. S. Jun, and T. H. Kwon, "Experiments on Chaotic Mixing in a Screw Channel Flow," *AIChE J*., **48**, 1621 (2002a).

Hwang, W. R., and T. H. Kwon, "Resonance and Invariant Advection in Single-Screw Extrusion," *Intern. Polym. Proc*., **17**, 309 (2002b).

Hwang, W. R., and T. H. Kwon, "Chaotic Volumetric Transports in a Single-Screw Extrusion Process," *Polym. Eng. Sci*., **43**, 783 (2003).

Jana, S. C., M. Tjahjadi, and J. M. Ottino, "Chaotic Mixing of Viscous Fluids by Periodic Changes in Geometry," *AIChE J*., **40**, 1769 (1994).

Kim, S. J., and T. H. Kwon, "Enhancement of Mixing Performance of Single-Screw Extrusion Process via Chaotic Flow: Part I. Basic Concept and Experimental Study," *Adv. Polym. Tech.*, **15**, 41 (1996).

Kusch, H. A., and J. M. Ottino, "Experiments on Mixing in Continuous Chaotic Flows," *J. Fluid Mech*., **209**, 463 (1992).

Mezić, I., and S. Wiggins, "On the Integrability and Perturbation of Three-Dimensional Fluid Flows with Symmetry," *J. Nonlinear Sci*., **4**, 157 (1994).

Ottino, J. M., *The Kinematics of Mixing: Stretching, Chaos, and Transports*, Cambridge U.K. (1989).

Rauwendaal, C., *Mixing in Polymer Processing*, Marcel Dekker, New York (1991).

Yao, W. G., S. Tanifuji, K. Takahashi, and K. Koyama, "Mixing Efficiency in a Pin Mixing Section for Single-Screw Extruder," *Polym. Eng. Sci*., **41**, 908 (2001).

Appendix: Symmetry in velocity field

We summarize below the symmetries in the velocity fields in all the types of this study, which should be incorporated to obtain the symmetries of the particle motion and, thereby, of the Poincaré map. We write the symmetries based on the particle location $\mathbf{p}=(x,y,\phi)$ using the reflection symmetries $\mathbf{s}_{y,\phi}$ and $\mathbf{s}_{x,y}$ defined in Eq. 7. (1) The symmetries in the basic types A, B, and C

$$\begin{aligned} u(\mathbf{p}) &= u(\mathbf{S}_{y\phi}\mathbf{p}) = u(\mathbf{S}_{xy}\mathbf{p}) = u(\mathbf{S}_{y\phi}\mathbf{S}_{xy}\mathbf{p}) \\ v(\mathbf{p}) &= -v(\mathbf{S}_{y\phi}\mathbf{p}) = v(\mathbf{S}_{xy}\mathbf{p}) = -v(\mathbf{S}_{y\phi}\mathbf{S}_{xy}\mathbf{p}) \\ w(\mathbf{p}) &= w(\mathbf{S}_{y\phi}\mathbf{p}) = w(\mathbf{S}_{xy}\mathbf{p}) = w(\mathbf{S}_{y\phi}\mathbf{S}_{xy}\mathbf{p}) \end{aligned} \tag{A1}$$

(2) The symmetries in the asymmetric types A1 and A2: Denoting the velocity of the type A1 by two distinct velocities $\mathbf{v}$ and $\mathbf{v}'$

$$\begin{aligned} u_{A1}(\mathbf{p}) &= u_{A1}(\mathbf{S}_{xy}\mathbf{p}) = u, \quad u_{A1}(\mathbf{S}_{y\phi}\mathbf{p}) = u_{A1}(\mathbf{S}_{y\phi}\mathbf{S}_{xy}\mathbf{p}) = u' \\ v_{A1}(\mathbf{p}) &= v_{A1}(\mathbf{S}_{xy}\mathbf{p}) = v, \quad v_{A1}(\mathbf{S}_{y\phi}\mathbf{p}) = v_{A1}(\mathbf{S}_{y\phi}\mathbf{S}_{xy}\mathbf{p}) = v' \\ w_{A1}(\mathbf{p}) &= w_{A1}(\mathbf{S}_{xy}\mathbf{p}) = w, \quad w_{A1}(\mathbf{S}_{y\phi}\mathbf{p}) = w_{A1}(\mathbf{S}_{y\phi}\mathbf{S}_{xy}\mathbf{p}) = w' \end{aligned} \tag{A2}$$

then the velocity components in the type A2 can be expressed again by $\mathbf{v}$ and $\mathbf{v}'$ as follows

$$\begin{aligned} u_{A2}(\mathbf{p}) &= u_{A2}(\mathbf{S}_{xy}\mathbf{p}) = u', \quad u_{A2}(\mathbf{S}_{y\phi}\mathbf{p}) = u_{A2}(\mathbf{S}_{y\phi}\mathbf{S}_{xy}\mathbf{p}) = u \\ v_{A2}(\mathbf{p}) &= v_{A2}(\mathbf{S}_{xy}\mathbf{p}) = -v', \quad v_{A2}(\mathbf{S}_{y\phi}\mathbf{p}) = v_{A2}(\mathbf{S}_{y\phi}\mathbf{S}_{xy}\mathbf{p}) = -v \\ w_{A2}(\mathbf{p}) &= w_{A2}(\mathbf{S}_{xy}\mathbf{p}) = w', \quad w_{A2}(\mathbf{S}_{y\phi}\mathbf{p}) = w_{A2}(\mathbf{S}_{y\phi}\mathbf{S}_{xy}\mathbf{p}) = w \end{aligned} \tag{A3}$$

where the velocity components of the type A1 are denoted by (u_{A1}, v_{A1}, w_{A1}) and of the type A2 by (u_{A2}, v_{A2}, w_{A2})..
(3) The symmetries in the oriented types C1 and C2:

The velocity components of these types can be expressed by two distinct velocities $\mathbf{v}$ and $\mathbf{v}'$

$$u(\mathbf{p}) = u(\mathbf{S}_{y\phi}\mathbf{S}_{xy}\mathbf{p}) = u, \quad u(\mathbf{S}_{y\phi}\mathbf{p}) = u(\mathbf{S}_{xy}\mathbf{p}) = u''$$

$$v(\mathbf{p}) = -v(\mathbf{S}_{y\phi}\mathbf{S}_{xy}\mathbf{p}) = v, \quad v(\mathbf{S}_{y\phi}\mathbf{p}) = -v(\mathbf{S}_{xy}\mathbf{p}) = v'$$
$$w(\mathbf{p}) = w(\mathbf{S}_{y\phi}\mathbf{S}_{xy}\mathbf{p}) = w, \quad w(\mathbf{S}_{y\phi}\mathbf{p}) = w(\mathbf{S}_{xy}\mathbf{p}) = w'' \tag{A4}$$

(4) The symmetries in the composite types A-B and C-B:

The symmetries in the composite types can be obtained in exactly the same form as in the basic types (Eq. A1), by using, $\bar{\phi}$, $\bar{\mathbf{S}}$ and $\mathbf{S}_{y,\ \bar{\phi}}$ (rather than ϕ, $\mathbf{S}_{xy}$ and $\mathbf{S}_{y\phi}$) defined in Eqs.13,14, because of the geometrical similarity. Details will not be repeated.

Manuscript received April 16, 2003, and revision received Sept. 15, 2003.